Tectonophysics 721 (2017) 56–69

Contents lists available at ScienceDirect

Tectonophysics

journal homepage: www.elsevier.com/locate/tecto

Ten kilometer vertical Moho offset and shallow velocity contrast along the Denali fault zone from double-difference tomography, receiver functions, and fault zone head waves

A.A. Allam[a,*,1], V. Schulte-Pelkum[b], Y. Ben-Zion[c], C. Tape[a], N. Ruppert[a], Z.E. Ross[c,d]

[a] Geophysical Institute, University of Alaska Fairbanks, Fairbanks, AK 99775-7320, United States
[b] Cooperative Institute for Research in Environmental Science, University of Colorado Boulder, Boulder, CO 80309, United States
[c] Department of Earth Sciences, University of Southern California, Los Angeles, CA 90089-0740, United States
[d] Seismological Laboratory, California Institute of Technology, Pasadena, CA 91125, United States

ARTICLE INFO

Keywords:
Denali fault
Moho offset
Fault zone structure
Suture zone tomography
Alaska tectonic history
Receiver functions

ABSTRACT

We examine the structure of the Denali fault system in the crust and upper mantle using double-difference tomography, P-wave receiver functions, and analysis (spatial distribution and moveout) of fault zone head waves. The three methods have complementary sensitivity; tomography is sensitive to 3D seismic velocity structure but smooths sharp boundaries, receiver functions are sensitive to (quasi) horizontal interfaces, and fault zone head waves are sensitive to (quasi) vertical interfaces. The results indicate that the Mohorovičić discontinuity is vertically offset by 10 to 15 km along the central 600 km of the Denali fault in the imaged region, with the northern side having shallower Moho depths around 30 km. An automated phase picker algorithm is used to identify ~1400 events that generate fault zone head waves only at near-fault stations. At shorter hypocentral distances head waves are observed at stations on the northern side of the fault, while longer propagation distances and deeper events produce head waves on the southern side. These results suggest a reversal of the velocity contrast polarity with depth, which we confirm by computing average 1D velocity models separately north and south of the fault. Using teleseismic events with M ≥ 5.1, we obtain 31,400 P receiver functions and apply common-conversion-point stacking. The results are migrated to depth using the derived 3D tomography model. The imaged interfaces agree with the tomography model, showing a Moho offset along the central Denali fault and also the sub-parallel Hines Creek fault, a suture zone boundary 30 km to the north. To the east, this offset follows the Totschunda fault, which ruptured during the M7.9 2002 earthquake, rather than the Denali fault itself. The combined results suggest that the Denali fault zone separates two distinct crustal blocks, and that the Totschunda and Hines Creeks segments are important components of the fault and Cretaceous-aged suture zone structure.

1. Introduction

The Denali fault (Fig. 1) is among the longest and oldest active strike-slip faults in the world; it has a total length of about 2000 km (Amand, 1957; Plafker and Berg, 1994; Fitzgerald et al., 2014) and has been active with the current right-lateral motion since at least the Cretaceous (Ridgway et al., 2002). A precursory zone of crustal weakness developed in the late Jurassic when an island arc assemblage collided with the North American margin (Nokleberg et al., 1994; Ridgway et al., 2002), creating a complex suture zone composed of accreted terranes, the Wrangellia Composite Terrane [WCT]. Oblique underthrusting of the northern edge of the WCT in the late Cretaceous (Nokleberg et al., 1985) gave way to predominantly right-lateral motion in the Paleocene (Plafker and Berg, 1994). Slip rates peaked in the Holocene at approximately 15 mm/yr, after which the slip has been consistent at the current rate of 10 mm/yr (Matmon et al., 2006; Biggs et al., 2007; Freymueller et al., 2008; Bemis et al., 2012). Total horizontal displacement estimates range from 200 km (e.g., Brogan et al., 1975) to 400 km (e.g., Nokleberg et al., 1985). Vertical displacement along the fault is highly variable; for example, the long-term uplift rate along the restraining McKinley segment has been approximately 10 mm/yr for the past 6 Ma (Fitzgerald et al., 1995), while estimates of vertical motion along other segments tend to be much lower or negligible (Stout and Chase, 1980).

* Corresponding author.
E-mail address: amir.allam@utah.edu (A.A. Allam).
[1] Now at Department of Geology & Geophysics, University Utah, Salt Lake City, UT 84112, United States.

http://dx.doi.org/10.1016/j.tecto.2017.09.003
Received 5 March 2017; Received in revised form 30 August 2017; Accepted 2 September 2017
Available online 09 September 2017

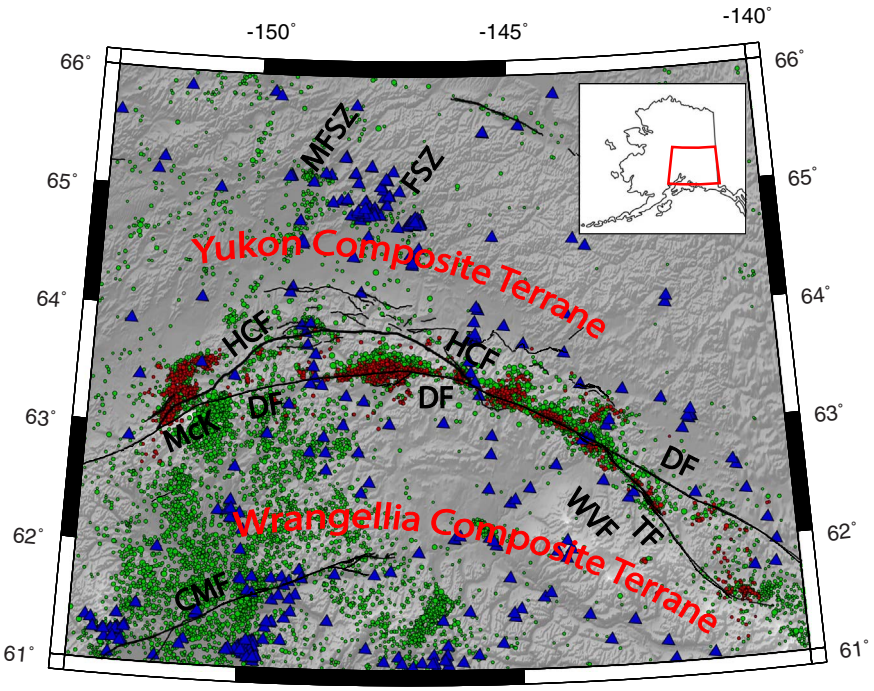

Fig. 1. Overview map of the Denali fault system showing the earthquakes used in the tomographic imaging (green circles) and the head wave analysis (red circles). Active faults from Koehler et al. (2012) are plotted, along with the Hines Creek fault (HCF) (Brennan et al., 2011; Bemis et al., 2015). Blue triangles are stations used in the tomographic inversion, which include networks AK, AL, PS, and Earthscope TA. Labels are: CMF-Castle Mountain Fault, DF-Denali Fault, FSZ-Fairbanks Seismic Zone, HCF-Hines Creek Fault, McK-McKinley Strand, MFSZ-Minto Flats Seismic Zone, TF-Totschunda Fault, WVF-Wrangell Volcanic Field. (For interpretation of the references to color in this figure legend, the reader is referred to the web version of this article.)

South of the suture zone, the WCT stretches from Vancouver to southwestern Alaska (Jones et al., 1977), but here we only discuss the central portion of the terrane. Before accretion, the WCT was an oceanic plateau consisting of a ~5 km thick Permian-aged flood basalt bounded above and below by marine sedimentary rocks (Richards and Jones, 1991). Since collision in the late Jurassic (Nokleberg et al., 1994; Ridgway et al., 2002), the WCT has been generally shortening parallel to the trench and accumulating subduction zone magmatic, volcanic, and sedimentary sequences (Jones et al., 1977; Jones et al., 1983). The entire terrane is currently rotating counter-clockwise, while also accommodating shortening across northeast-southwest structures (Freymueller et al., 2008) such as the Castle Mountain Fault system (Fig. 1); biogeographic constraints suggest that this rotation is relatively recent (Aberhan, 1999). In addition, uplift rates measured geodetically change dramatically across the Denali fault system, with the southern side uplifting at 6 mm/yr relative to the northern side (Freymueller et al., 2008). Much of the WCT imaged in the present study is underlain by subducted Pacific Plate from the Alaskan subduction zone to the south. The southern Alaskan margin has undergone subduction since the early Triassic (Rioux et al., 2010), and continues obliquely today in a north-northwesterly direction at ~55 mm/yr (Freymueller et al., 2008; Argus et al., 2010). Subduction of the Yakutat microplate to the southeast and along the Aleutian arc to the southwest are outside the scope of the present work.

The north side of the Denali fault is composed of the complexly deformed metamorphic and plutonic rocks of the Yukon Composite Terrane [YCT]. The bulk of the YCT formed through repeated episodes of continental arc magmatism, with the three main pulses beginning in the late Devonian, middle Permian, and late Triassic (Mortensen, 1992; Plafker and Berg, 1994). Jurassic crustal thickening, which resulted from the accretion of the WCT in the late Jurassic (Nokleberg et al., 1994; Ridgway et al., 2002), was followed by mid-Cretaceous extension (Hansen, 1990; Pavlis et al., 1993) possibly due to outboard trench migration (Dusel-Bacon et al., 2002). This extension was accompanied by crustal thinning, uplift, erosion, and further magmatism (Aleinikoff et al., 1986; Pavlis et al., 1993; Dusel-Bacon et al., 2002). Though relatively stable since Cretaceous time, the western part of the YCT exhibits small variations in GPS motions (Freymueller et al., 2008) and diffuse seismicity. East of the junction between the Denali and Hines Creek faults (Fig. 1), the boundary between the WCT and YCT is marked sharply by the Denali fault zone. West of this junction, the suture zone consists of a complicated assemblage of Paleozoic to Cretaceous sedimentary strata (Ridgway et al., 1997; Brennan et al., 2011) intruded by Quaternary plutons (Plafker et al., 1992). The complex deformation and uplift patterns associated with the Denali fault in this area–especially the McKinley Strand (Fig. 1)–are likely controlled by the heterogeneity of rock strength (Fitzgerald et al., 2014).

Previous seismic imaging studies of the Denali fault have focused on the large-scale structure of the subduction zone. Body-wave tomographic studies using local earthquakes (Kissling and Lahr, 1991; Eberhart-Phillips et al., 2006) and teleseismic earthquakes (Qi et al., 2007; Martin-Short et al., 2016) have successfully imaged slab structure that is consistent with the Wadati-Benioff seismicity patterns. Teleseismic surface-wave wave tomography (Wang and Tape, 2014) of the entire state employed ~50 km horizontal cells to image upper mantle structure. Surface-wave phase velocity maps derived from ambient noise show crustal variations, including a possible contrast across the Denali fault (Ward, 2015). These large-scale studies did not achieve sufficient resolution to image crustal heterogeneity.

More focused transects in the central portion of the current study area have yielded higher-resolution two-dimensional cross-sections. Numerous studies, starting with Ferris et al. (2003), have used receiver functions from the Broadband Experiment Across the Alaska Range (BEAAR) deployment (Christensen et al., 1999) to estimate Moho depth across the Denali fault. These studies reveal a sharp contrast in the Moho across the Hines Creek fault, a structure about 25 km north of the Denali fault (e.g., Brennan et al., 2011; Wang and Tape, 2014, Fig. S3). Geological mapping has led to the interpretation that the northern boundary of the WCT-YCT suture zone is along the Hines Creek fault (Wahrhaftig et al., 1975). Recent studies reveal some near-vertical offsets but no lateral offsets along the Hines Creek fault (Bemis et al., 2012; Bemis et al., 2015); the structure was considered for but omitted from the active fault map for Alaska (Koehler et al., 2012). Active-source seismic and other combined geophysical methods used in the TACT (Trans-Alaskan Crustal Transect) deployment 150 km to the east, near the junction of the Denali and Hines Creek faults, suggested a more gradual change in Moho depth north of the fault (Brocher et al., 2004; Fuis et al., 2008). Further to the east, the Denali fault's southeastward

branch, the Totschunda fault (Fig. 1), is currently seismically active and accommodated the eastern portion of rupture during the 2002 M7.9 Denali earthquake (Eberhart-Phillips et al., 2003). The subsurface structure of the Totschunda fault is unknown, and it is a matter of debate whether the more tectonically active segment is the Totschunda or eastern Denali fault (e.g., Bhat et al., 2004; Doser, 2004). Determining the relative structural importance of the Totschunda and Hines Creek fault strands is one of the goals of the present work.

These disagreements about Moho depths and the importance of different fault segments, likely stemming from differences in data and varying station geometries, in part motivate the present study. In addition, data availability and recent methodological advances allow for dramatically improved 3D seismic imaging results. Hundreds of stations and tens of thousands of events distributed throughout the study area provide ample volumetric sampling for high-resolution tomographic methods which have previously been applied to image fault and regional structure elsewhere (e.g., Zhang and Thurber, 2003; Allam and Ben-Zion, 2012; Bennington et al., 2013; Allam et al., 2014a). Migration of receiver functions using accurate 3D seismic velocity models has been shown to change interpretations (Gilbert, 2012; Hansen et al., 2013; Ozakin and Ben-Zion, 2015). Finally, fault zone head waves refracting along an interface separating different crustal blocks provide direct evidence for sharp contrasts of seismic velocities across faults (e.g., Ben-Zion, 1989, 1990). For near-fault earthquakes recorded at stations sufficiently close to the fault in the slower material, head waves are observed as an emergent first arrival with opposite polarity to the direct P wave (e.g., Ben-Zion et al., 1992; McGuire and Ben-Zion, 2005). Newly developed automated phase picking (Ross and Ben-Zion, 2014) and particle motion (Bulut et al., 2012; Allam et al., 2014b) methods allow for precise measurement of head wave travel times.

The goal of the present work is to image the Denali fault and related structures such as the Hines Creek and Totschunda faults that operate as part of the same system. We employ three methods that have complementary sensitivity: double difference tomographic imaging is sensitive to 3D seismic velocity, receiver functions are sensitive to near horizontal interfaces within and below the crust, and fault zone head waves are sensitive to near vertical interfaces in the fault zone structure. We combine all the available seismic data, including the BEAAR (Christensen et al., 1999), TACT (Brocher et al., 2004), Earthscope Transportable Array (Meltzer et al., 1999), and regional Alaska seismic network stations. Fault zone head wave analysis has not previously been applied to the Denali fault. Receiver functions and tomography have been performed previously in this region (Ferris et al., 2003; Eberhart-Phillips et al., 2006), but the present study incorporates a greatly expanded dataset and additional constraints such as migration of the receiver functions through a 3D seismic velocity model. Tomographic methods have been applied only at the large scale with horizontal resolution in the tens of kilometers. The combined imaging done in this study provides the highest resolution models of seismic velocities currently available for the region.

2. Methods and data

In this section, we describe the three methods used in this work to image the seismogenic crustal structure of the Denali fault and surrounding region, along with the corresponding data sets.

2.1. Double-difference tomography

Double-difference tomography makes use of local earthquake arrival time data to simultaneously invert for P velocity, S velocity, and hypocenter location (Zhang and Thurber, 2003). In the present work, we use P and S wave arrival time data from 15,880 events obtained from the Alaska Earthquake Center catalog with the following search ranges: 2003–2015, Mw > 2.0, depth ≤ 55 km, longitude −153 to −140, latitude 61 to 66. These events were recorded at 326 stations in the permanent networks, past temporary networks, and EarthScope Transportable Array (Fig. 1). With an average of 45 P and 15 S arrival times per event, we use a total of 715,000 P and 230,000 S arrival times. Grouping events with hypocentral distances < 2 km apart, we compute 845,500 differential P and 224,000 differential S travel times. The maximum event depth is 55 km, which is well above the subducted Pacific Plate in the vicinity of the Denali fault. The arrival time data were obtained from the Alaska Earthquake Center (AEC) and contain a mix of both automatically generated and analyst-reviewed phase arrival picks. Events and stations are well-distributed to provide good volumetric coverage for the tomographic inversion. The events are associated with multiple structures, including the Denali fault, Totschunda fault, downgoing Alaskan subduction zone slab, and various faults within both the Yukon and Wrangellia composite terranes. The stations are a mixture of broadband, strong motion, and temporary deployments.

We discretize a 600 km × 560 km × 70 km region around the central Denali fault with 5 km uniform horizontal and a 3 km vertical grid spacing. Following previous applications (Zhang and Thurber, 2003; Thurber et al., 2006; Allam and Ben-Zion, 2012; Allam et al., 2014a), we perform 35 iterations with a progressive weighting scheme between absolute and differential arrival time data. In the first few iterations, the absolute arrival time data are weighted more importantly by a factor of 10. At the 18th iteration, the weighting is a factor of 10 towards the differential data. This weighting scheme establishes the broad-scale velocity structure in the early iterations while converging to a stable result incorporating higher-resolution differential times by the final iteration. An iterative inversion scheme is necessary because the inversion is non-linear; the ray paths, which depend on the velocity structure, are recalculated for each iteration.

The derivative weight sum (DWS) is a measure of the sensitivity of each inversion node to changes in seismic velocity (Thurber and Eberhart-Phillips, 1999), and is generally proportional to the density of ray-paths near each inversion node. To improve inversion results, we exclude nodes with low DWS values from the inversion; this prevents velocity anomalies from being distributed along the inversion boundaries. Because they provide a general estimate of resolution, we show contours of DWS values of 10 on plots of Vp and Vs in order to guide interpretation. Though this value is ad hoc, in practice the gradient of DWS is steep and interpretation of results is not sensitive to the particular value chosen (Zhang et al., 2004; Allam and Ben-Zion, 2012; Allam et al., 2014a).

2.2. Receiver functions, Moho picks, and common conversion points (CCP) stacking

Receiver functions are a result of removing the source signature from teleseismic arrivals—in this case P and P_{diff}—to highlight near-station conversions from P to S. Conversions are generated at isotropic Vs contrasts as well as contrasts in Vp anisotropy (Park and Levin, 2016). While generally the arrival time of the converted phase scales to depth, and can be migrated to depth if the Vp and Vs structure between the converted and receiver are known, reverberations between shallower interfaces and the free surface can interfere with converted arrivals from a deeper interface (e.g. Yeck et al., 2013). This effect is particularly pronounced at stations located in or near basins. In tectonically active areas, receiver function arrivals can show a strong dependence on event backazimuth (Schulte-Pelkum and Mahan, 2014a, 2014b), and uneven sampling generated by the azimuthal distribution of seismicity can bias the local 1-D structure inferred from radial component receiver functions.

The receiver function analysis uses data from three-component stations from permanent stations of the Alaska network, previous temporary deployments including BEAAR (Meyers et al., 2000), and recently installed EarthScope Transportable Array stations. We incorporate all available data from these stations for the time range 1980

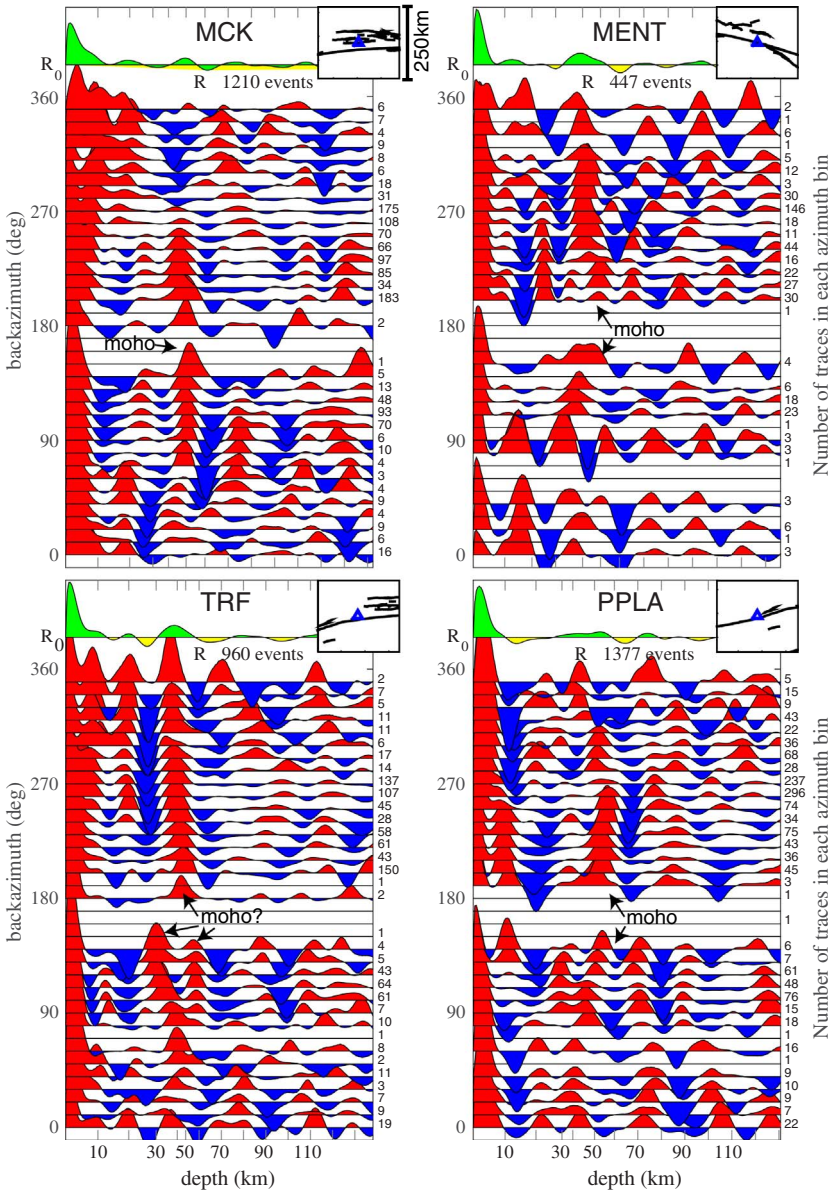

Fig. 2. Receiver function stacks as a function of event backazimuth for four different stations (MCK, MENT, TRF, PPLA). Insets show station locations relative to fault structure; larger-scale station locations are shown in Fig. 4a. The x-axis is linear in delay time, with nonlinear depth ticks (marked every 10 km) because of variations in Vp and Vs in the velocity models used for depth migration. Traces are corrected for incident slowness before stacking. Number of events per bin shown on right of traces. Azimuthal average stack R0 shown on top. All four near-fault stations show azimuthal dependence to the perceived Moho depth; arrivals from the North produce shallower Moho estimates than arrivals from the South (backazimuth 90–270). In addition, sedimentary basins near MCK (top left) add complexity, completely erasing the Moho arrival from some backazimuths.

to 2016. For each station, we calculate receiver function for all available events of Mw > 5.1 and at epicentral distances of 28° to 150° using the time-domain iterative method of Ligorría and Ammon (1999) with a Gaussian filter value of 3. High-quality receiver functions are selected via an automated process described in detail in Schulte-Pelkum and Mahan (2014a), with minimum criteria for signal-to-noise ratio of the raw vertical component, variance reduction of the deconvolved time series, and amplitude and pulse length requirements, all to ensure stable deconvolutions. After the quality control steps, we obtain a total of 31,408 radial component receiver functions at 114 stations.

2.2.1. Moho depths

The radial component receiver functions show significant azimuthal variations at the majority of the stations (examples are shown in Fig. 2 for stations situated on or near the Denali fault). We correct the receiver functions for time shifts as a function of slowness, stack them in azimuthal bins, and calculate an azimuthal average to pick the Moho conversion with the least possible bias from azimuthal variations. Moveout with slowness is also considered during picking, and Moho picks are not taken at stations with strong basin overprints. At each station, local 1-D Vp and Vs velocity models derived from the tomography described in Section 2.1 are used to convert the Moho delay time to depth below sea level. At some stations, especially above the slab, the Moho is not the strongest conversion. When several interfaces are present, we seek coherence with neighboring stations to select the Moho.

2.2.2. Cross sections for Moho and subducted slab structure

We show two different common conversion point (CCP) stacks projected on N-S oriented profiles (Fig. 3; stations used are shown in Fig. S6). The basic procedure is the same as in Hansen et al. (2013). Receiver functions are projected to depth using the 3-D Vp and Vs velocity models from the tomographic inversion in Section 2.1. Rather than choosing a full 3-D raytracing treatment, we use the 1-D velocity Vp and Vs models under each station; because of the inherent smoothness of the tomographic models and the steep incidence of the rays, a fully 3-D treatment would not significantly impact the results. We project data onto the profile along an E-W swath with varying widths of the projection depending on the imaging target. The first image (Fig. 3a) targets the Moho, and we use stations in a 250 km wide swath perpendicular to the profile, but exclude stations which show patterns of shallow basin reverberations, in order to optimize ray

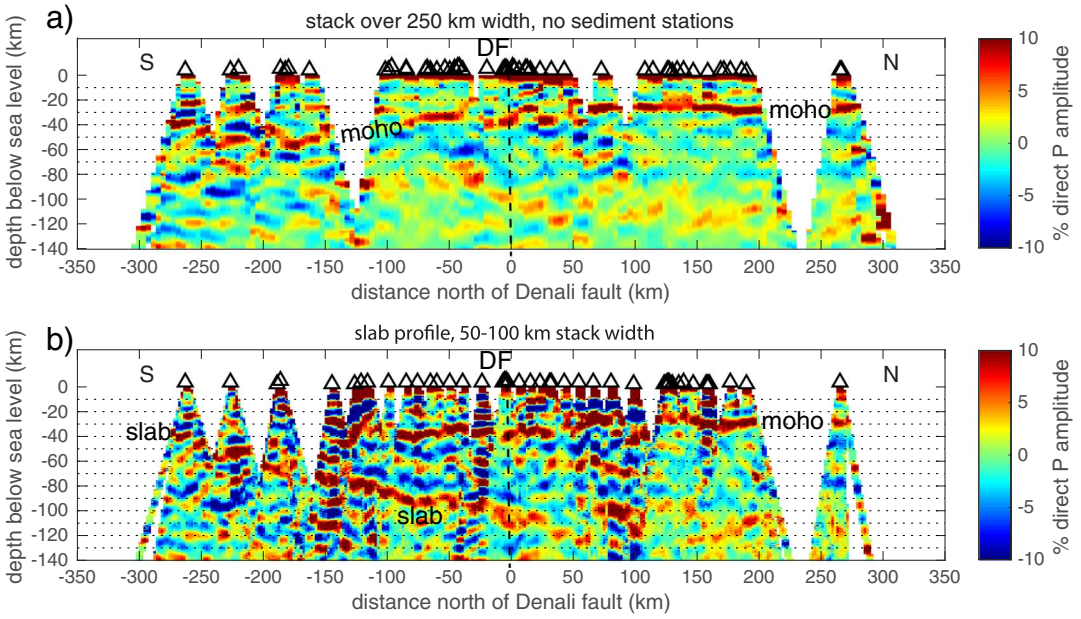

Fig. 3. Migrated receiver function common conversion point (CCP) stacks. (a) Moho depth. Though there is some noise due to shallow (< 5 km) structure north of the Denali fault, there is a moho offset 10 km north of the fault and consistently shallower moho north of the fault. (b) Subducted slab geometry. The continuous slab structure demonstrates that the offset in (a) is introduced by shallow structure.

coverage at Moho depths without reverberation overprint. Since the slab dips obliquely to the profile, the wide profile (profile shown in Fig. S6) results in decorrelation of its conversion. The second image (Fig. 3b) targeting the slab is therefore constructed using a narrower cross-profile width (100 km width; Fig. S6) following a line of densest possible station coverage to obtain a much sharper image of conversions from the slab. In this case, basin stations are included; shallow multiples are seen within the crust, and some reverberation ghosts follow the Moho and slab arrivals, but the strongest deep conversions are separated from the shallow reverberations. The actual regions used for the projections are shown in Fig. S6 (yellow and orange lines for Moho and slab profiles respectively). We minimize horizontal smoothing in both cases and use narrow along-profile bins to avoid smearing structure.

2.3. Fault zone head waves (FZHW)

FZHW are associated with emergent arrivals on the slower side of a (near) vertical lithology contrast interface, which precede the more impulsive regular body waves for stations located sufficiently close to the fault (e.g., Ben-Zion, 1989, 1990). The presence of FZHW indicates a contrast of seismic velocities across the fault, while their absence indicates that there is not a (sufficiently sharp) across-fault contrast. We apply the automated algorithm of Ross and Ben-Zion (2014) to waveforms generated by 1838 near-fault events using statistical properties of waveforms, short-term-average compared to long-term-average amplitude (STA/LTA), kurtosis and skewness to detect and obtain picks of FZHW arrival times. We verify some of the head wave picks with visual inspection and using particle motion analysis (Bulut et al., 2012; Allam et al., 2014b). The automated detection algorithm differentiates between P and head waves using a multistage process that accounts for the characteristics of the two phases, including motion polarities, time difference, impulsivity, and amplitude. The first stage makes a pick of the onset of seismic motion above the noise. The second stage identifies the direct P arrival using kurtosis and skewness, both of which are most sensitive to abrupt (i.e., impulsive) changes in the seismic timeseries, such as occur at the onset of a P wave. The FZHW, if present, is identified as an emergent first arrival with opposite polarity to the direct P wave and a relatively short time difference. For a more detailed discussion of the automated method, including sliding time window lengths and detection thresholds, see Ross and Ben-Zion (2014).

Because head waves propagate along a velocity contrast interface, and are radiated from the interface to the slower side of the fault, they are the first-arriving phase at near-fault stations in the slower material. To validate the automated algorithm, we apply it to a subset of 112 events over the entire regional array (Fig. 4a); the algorithm uses only statistics of waveforms and makes no assumptions involving source-receiver geometry. Other than a few spurious false positives at southern stations, the algorithm only picks head waves at near-fault stations. This pattern, in line with theoretical (e.g., Ben-Zion, 1989) and observational (e.g., Lewis et al., 2007) expectations, provides confidence that the results of the automated algorithm are generally correct. We visually confirm that the flagged FZHW are similar to head waves observed at other fault systems (e.g. Allam et al., 2014b). After this validation step, we apply the algorithm to the larger catalog of 1838 near fault events (Mw > 2.5) using only the near-fault stations (Fig. 4b).

As a further check on their validity, we examine the horizontal particle motion of several head wave picks using 3-component seismograms (Supplementary material). During the first onset of seismic motion, the horizontal particle motion polarity changes from essentially random (noise) to approximately fault-normal (head wave) direction and then to epicentral (direct P wave) orientation. Combined with changes in amplitude (emergent for head and impulsive for direct waves), this property has previously been used to identify head waves on the North Anatolian (Bulut et al., 2012; Najdahmadi et al., 2016), Hayward (Allam et al., 2014b), and Southern San Andreas (Share and Ben-Zion, 2016) faults. Because this analysis is not automated (and time consuming), we only apply it to a few events to verify the automated picks.

3. Results

3.1. P and S velocity models

Our tomographic models derived from P and S arrival time data is presented in Figs. 5 and 6. Fig. 5 shows map-view depth slices of Vp (left), Vs (middle), and Vp/Vs ratio (right) for different depths relative to sea level with white contours enclosing well-resolved areas with

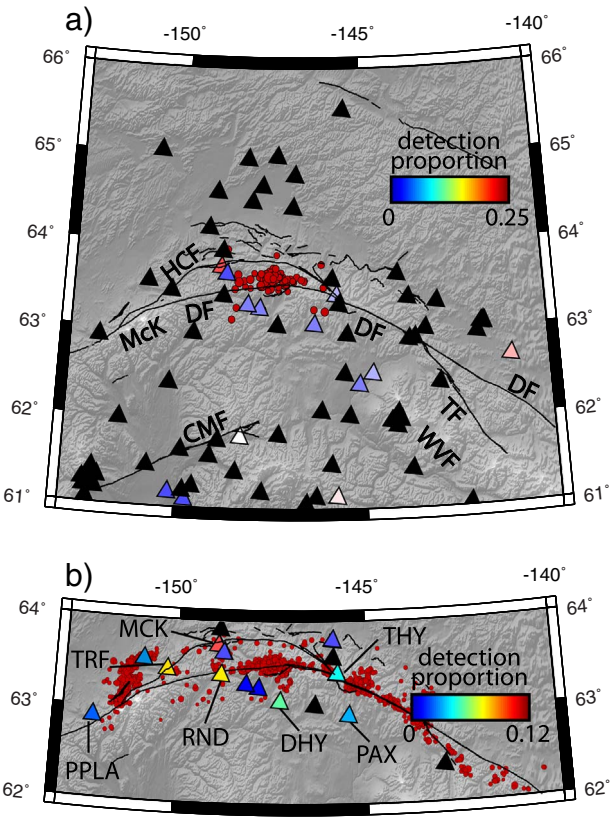

Fig. 4. Summary of the automated head wave detections for the entire array (top), and for a more focused subset of near-fault stations using more events. Red circles are earthquakes, and triangles are stations colored by the percentage of head wave detection. See Section 3.4 for details. (For interpretation of the references to color in this figure legend, the reader is referred to the web version of this article.)

DWS higher than 10. Fig. 6 shows cross-section views through the same models. Due to the lower number of phase picks used and the generally greater uncertainty in arrival time picks, the Vs model has slightly lower resolution than the Vp model and has some streaking artifacts visible below 45 km. However, the Vp/Vs ratio model is stable at all depths, showing only minor fluctuations, which we interpret to represent variations in crustal composition. The absence of strong artifacts suggests that the Vs model resolution is not significantly lower than the Vp model (e.g., compared to Allam and Ben-Zion, 2012; Fig. S3 therein).

The most prominent feature in both Vp and Vs is the contrast in velocity across the Denali fault at 30 km and below (Fig. 5 left bottom), with near-fault Vp at ~6.7 km/s on the south side and ~7.7 km/s on the north side. This pattern is consistent along the entire length of the fault except the easternmost imaged section, where the velocity contrast follows the southern-branching Totschunda fault (Fig. 5). Below 50 km, this contrast disappears as both sides have similar upper mantle velocities of ~7.8 km/s (Fig. 6). Interestingly, at shallower depths the velocity contrast across the fault has the opposite polarity; the north side has slightly lower velocities near-fault at depths < 20 km (Fig. 5 top left). The provenance of other signals is unclear; the lowest velocities in the entire model in both Vp and Vs occur near Wrangell Volcanic Field (Fig. 1), while very high shallow velocities occur just to the north and west in the center of the WCT.

To assess the approximate spatial resolution of the tomographic results, we perform checkerboard tests (Fig. 7). In the first model, we apply 70 km checker-shaped anomalies to a homogeneous base. For the second model, we start with a simple 1D gradient increasing with depth and then add evenly spaced anomalies at 15 km horizontally and 6 km vertically. Both models use alternating amplitudes of ± 0.5 km/s for the anomalies. After computing travel times for all of the employed phases, we impose random Gaussian noise with half-width 50 ms. Using this dataset, we then invert starting from a 1D model with no horizontal variation. For both test models, anomaly recovery is high throughout the well-resolved (DWS > 10) region at all depths, providing confidence in the Vp and Vs models presented above. The boundaries between the anomalies are preserved during the test, suggesting that resolution is likely much better than the size of the anomalies. In particular, we note that the region between the Denali and Hines Creek faults are very well-resolved, with sharp boundaries preserved for the larger-scale test (top) and several multiple anomalies recovered for the smaller-scale test (bottom). Though checkerboard tests are a useful step to provide some guidance in the interpretation of tomographic models, they cannot be directly used to calculate resolution (e.g., Lévêque et al., 1993). This is because the actual paths taken by the seismic waves used in the inversion are actually dependent on the structure itself. Checkerboard tests thus provide only a general sense about the size of features which can be reasonably interpreted from the seismic data. Nevertheless, the results of this test lead us to conclude that all the discussed features in Figs. 5 and 6 are well-resolved.

3.2. Hypocenter locations

The double-difference tomography method inverts for earthquake location along with the seismic velocity structure. Fig. 8 compares the final relocated (green) and initial (blue) epicentral locations. In general, the relocated events cluster slightly more tightly around the mapped fault traces and in some places, such as the Fairbanks and Minto Flats seismic zones (Fig. 1), delineate unmapped structures. These seismicity patterns are in agreement with previous relocation studies of the Denali Fault (Ratchkovski et al., 2004; Ruppert et al., 2008). The mean difference from initial to final locations is 3.6 km horizontally and 2.6 km vertically, with standard deviation 4.0 km and 3.75 km respectively. The total distribution of location changes is shown in Fig. 9. Given that the initial locations were derived from a 1D model and that the final 3D model shows strong lateral heterogeneity, these large changes in location are reasonable.

Several interesting seismicity patterns are shown in Fig. 8; locations are labelled in Fig. 1. In the Fairbanks Seismic Zone (Fig. 8a), initially diffuse catalog seismicity has been relocated along several northeast-southwest trending structures, the most notable being the two strands of the Minto Flats fault zone (Tape et al., 2015). The Denali Fault just west of the Totschunda branch (Fig. 8b) is dominated by aftershocks of the 2002 M7.9 earthquake. The aftershocks are asymmetrically distributed, with more on the north than south side of that fault. To the east (Fig. 8d), the aftershocks follow the southern-branching Totschunda fault and are absent from the northern branch of the Denali fault. The McKinley Strand manifests (Fig. 8c) as a band of diffuse seismicity known as the Kantishna cluster (Ratchkovski and Hansen, 2002). An interesting cluster of seismicity is observed just west of the Wrangell Volcanic Field (Fig. 1) in the same region as the lowest Vp and Vs velocities (Fig. 5).

3.3. Receiver functions

Fig. 10 shows Moho picks from receiver functions after correction for azimuthal bias and migration to depth using the tomographic Vp and Vs models. A large-scale pattern is one of shallow Moho depths in the southern and northern parts of the study area, with deeper Moho picks concentrated south of the Denali fault. A shallowing of the Moho north of the Denali fault is consistent with the tomographic results showing a velocity contrast across the fault at 30–45 km depth (Figs. 5 and 6).

The change in depth of the Moho in the vicinity of the Denali fault is also visible in the CCP stack (Fig. 3a). From ~90 km south of the fault to ~30 km south of the fault, the Moho appears as a clear and simple

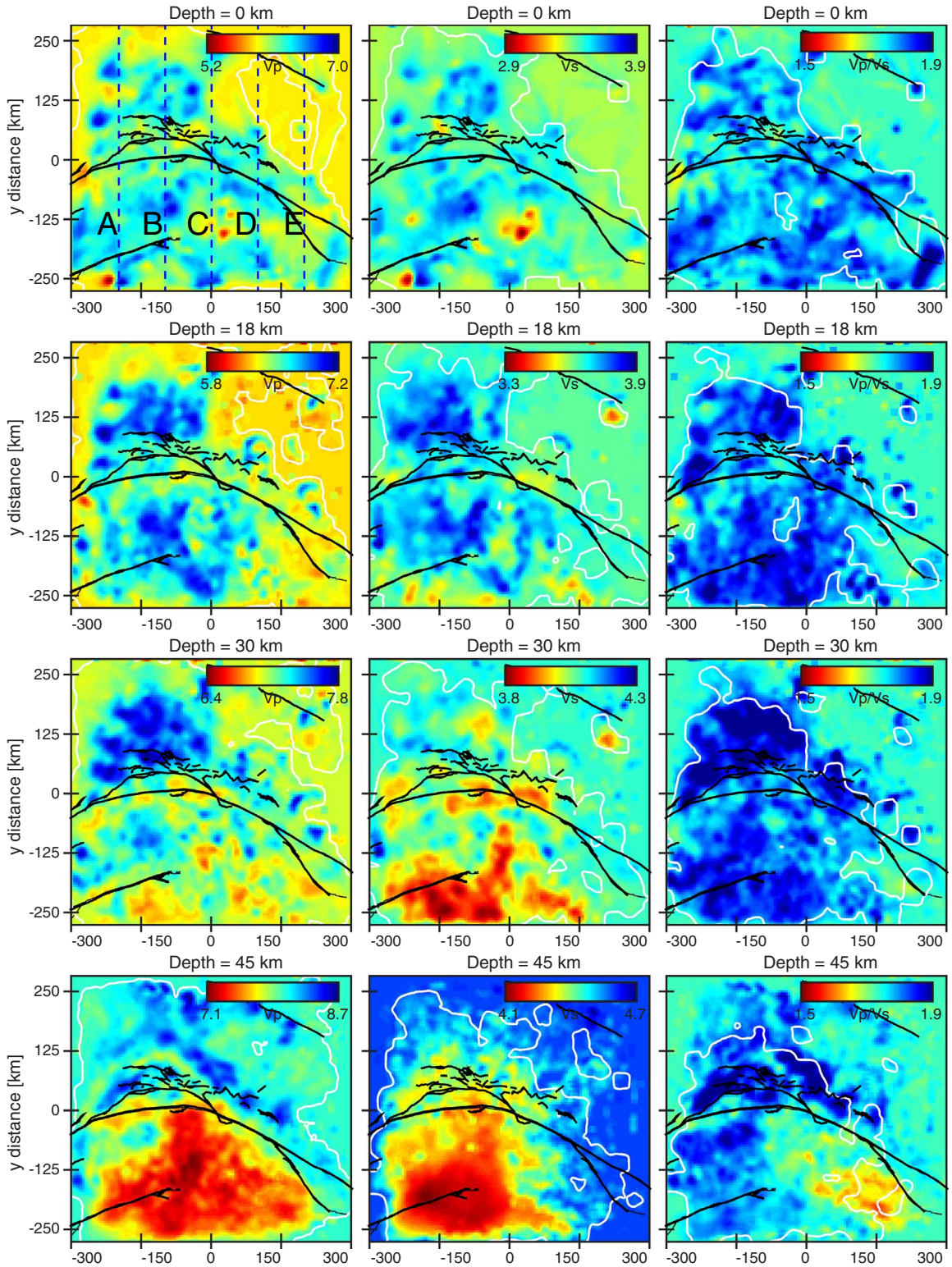

Fig. 5. Map-view cross-sections of Vp (left), Vs (middle), and Vp/Vs (right) are shown at four different depths (rows top to bottom: 0 km, 18 km, 30 km, 45 km depths). The Vp (left) and Vs (middle) columns are the results of inversion of separate datasets; the Vp/Vs ratio (right) is just Vp/Vs at every location. White contours enclose areas considered well-resolved based on the derivative weight sum. Higher velocities (blue) generally indicate either more rigid or colder rocks compared to lower velocities (red) which indicate lower rigidity or rocks at higher temperature. Above 18 km, the YCT (northern) side of the Denali fault has slower velocities. At 30 km and below, the mantle velocities of the YCT are faster than the crustal velocities of the Wrangellia on the southern side of the fault system, which includes the Hines Creek and Totschunda faults (see Fig. 1 for fault location labels). (For interpretation of the references to color in this figure legend, the reader is referred to the web version of this article.)

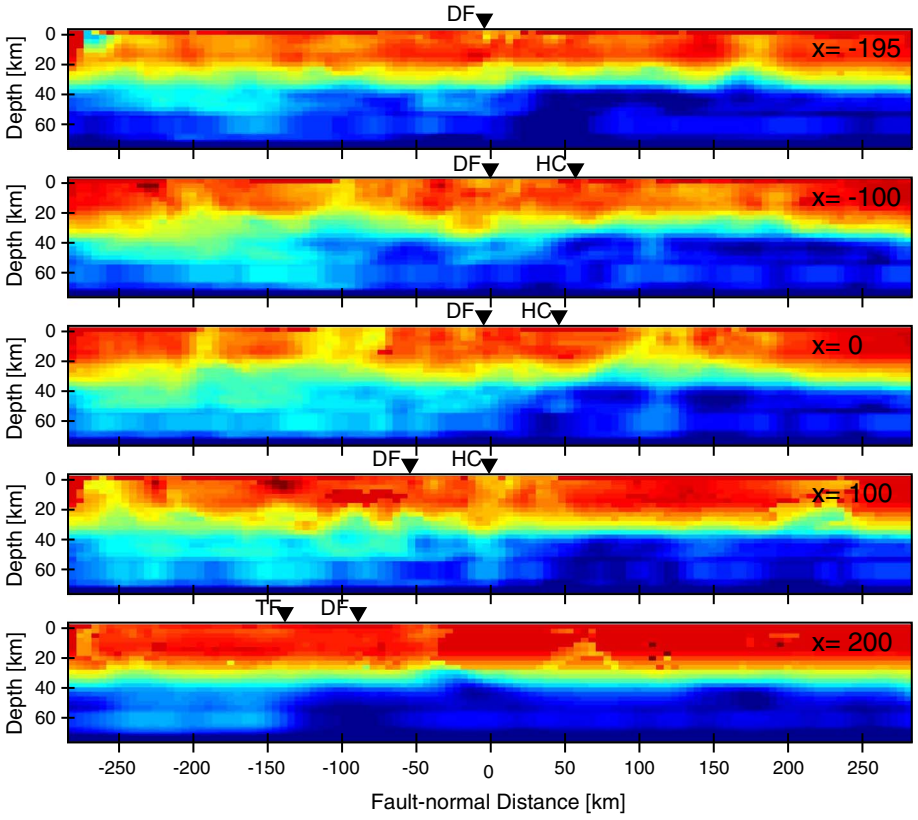

Fig. 6. Vertical N-S cross-sections of Vp shown from west (top) to east (bottom). Refer to Fig. 5 (top left) for profile locations. The offset Moho is prominent in all of the cross-sections, and coincides approximately with the surface trace of the Denali and Totschunda faults. Labels: DF-Denali Fault, HC-Hines Creek Fault, TF-Totschunda Fault.

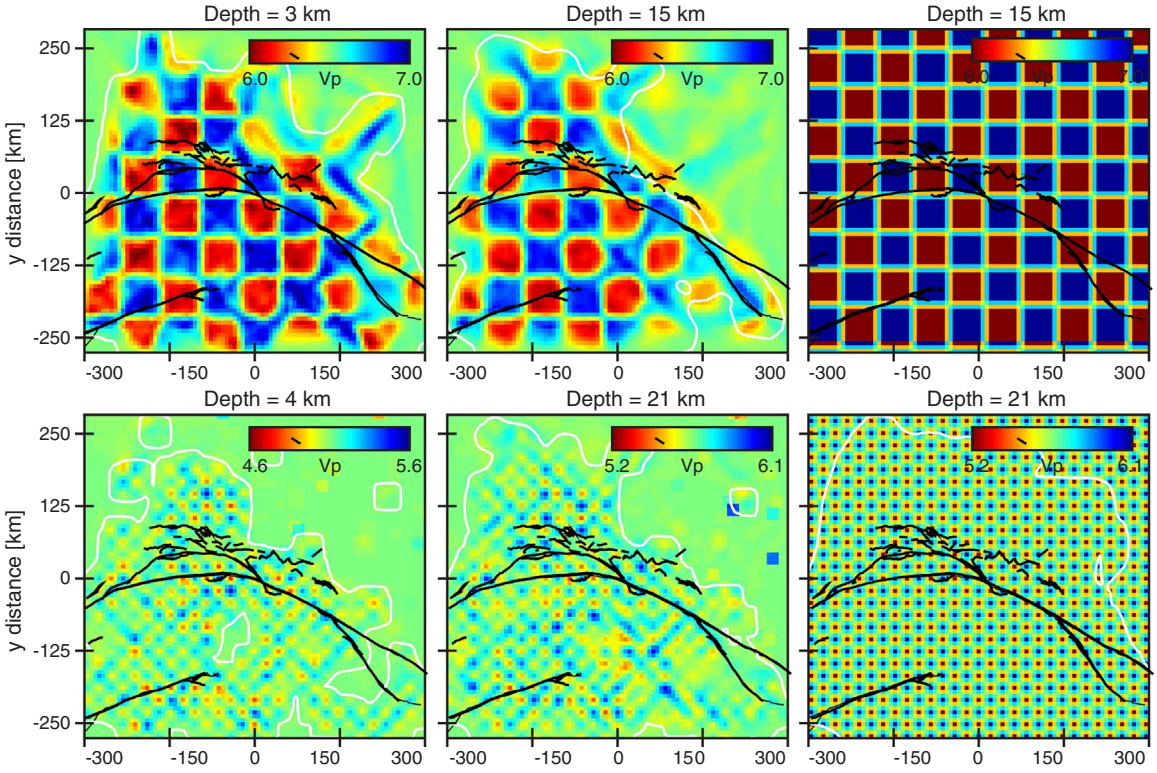

Fig. 7. Map-view cross sections of coarse 20 km (top row) and fine 7 km (bottom row) checkerboard tests. The true models are shown on the right. Within the resolved area, the models are well-recovered at both coarse and fine scales.

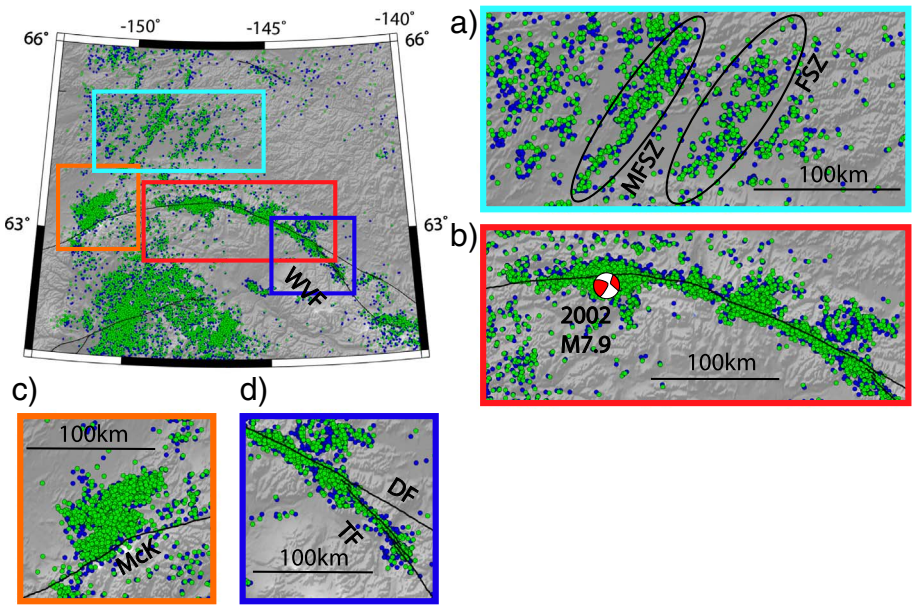

Fig. 8. Earthquake epicenter locations from the original Alaska Earthquake Center catalog (blue) compared to the double-difference relocations (green). In general, the relocations cluster more tightly around fault structures and align along the seismic zones in the northern YCT. See text (Section 3.2) for details. (For interpretation of the references to color in this figure legend, the reader is referred to the web version of this article.)

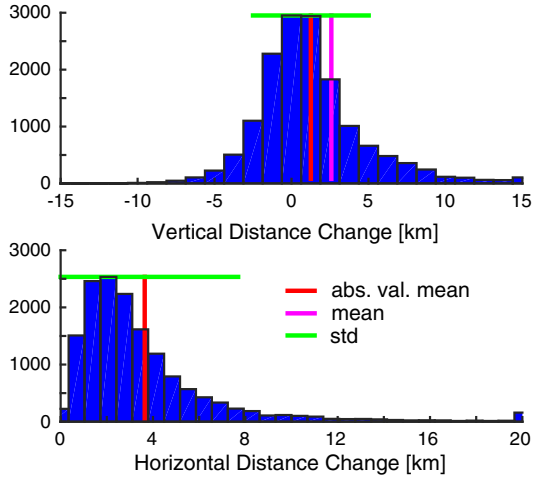

Fig. 9. Distributions of vertical (top) and horizontal (bottom) hypocenter relocations from the double-difference tomographic inversion. The total number of earthquakes is 15,880.

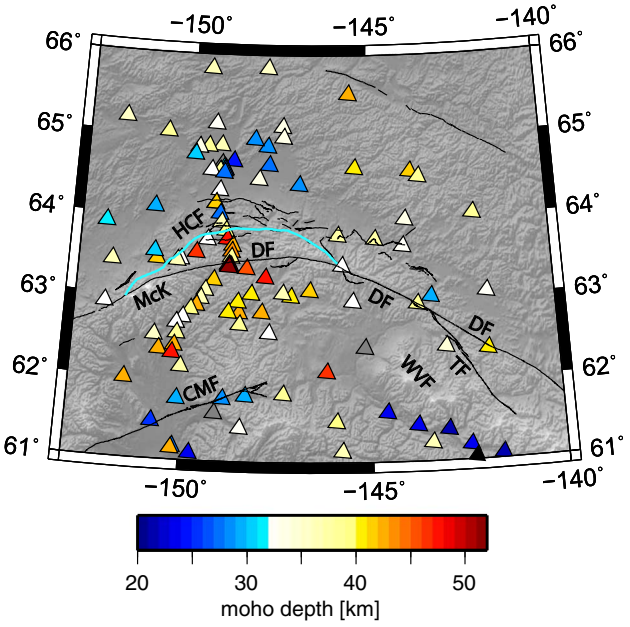

Fig. 10. Map of the Moho depth inferred from the stacked receiver functions at each station. In general, the YCT has shallower Moho depths, while the WCT has deeper Moho arrivals. The Hines Creek fault (cyan) accommodates the sharpest Moho offset. (For interpretation of the references to color in this figure legend, the reader is referred to the web version of this article.)

conversion at ~35 km depth. Between ~60–300 km north of the Denali fault, the Moho has a similarly simple appearance, with depth mostly near 25 km. The imaged structure is less simple within ~50 km of the Denali fault. Multiple conversions shallower than the moho are inconsistent from station to station, possibly due to highly heterogeneous shallow structure which can bias depth interpretation of the moho. The raw receiver functions from this region are complicated (Fig. 2, station MCK) and do not allow for unique interpretations of moho depth. However, a step of ~10 km upwards to the north, located < 10 km north of the surface trace of the fault, appears to correspond to the velocity contrasts seen at 30–45 km depth in the tomographic results in Fig. 3. Imaging depth is most strongly controlled by Vp/Vs ratio, which does not show a large variation across the fault at crustal depths (Fig. 3), so that migration with constant velocities does not remove the Moho step.

The slab can be traced from the southern end of the profile to about 60–80 km north of the Denali fault (Fig. 3b), where it has a depth of ~125 km. Because the tomographic inversion only constrains velocities to 50 km depth, receiver functions are migrated with constant assumed mantle Vp and Vs. The image of the slab shows a near-constant apparent dip. The true dip of the slab is somewhat steeper, since the dip direction is oblique to the N-S projection in Fig. 3 (Hayes et al., 2012).

3.4. Fault zone head waves

Fig. 4 summarizes the detection results of the automated head wave picking algorithm. Fig. 4a shows the control group of events which were analyzed using the entire array. There are a few stations far away from the fault which produce spurious head wave picks (described below), but largely the picks are confined to the near-fault stations on both sides of the surface trace of the fault. Fig. 4b shows the results for all events recorded at near-fault stations, with the station colors corresponding to the proportion of head waves detected relative to the number of events used at each station (minimum 100 events). The

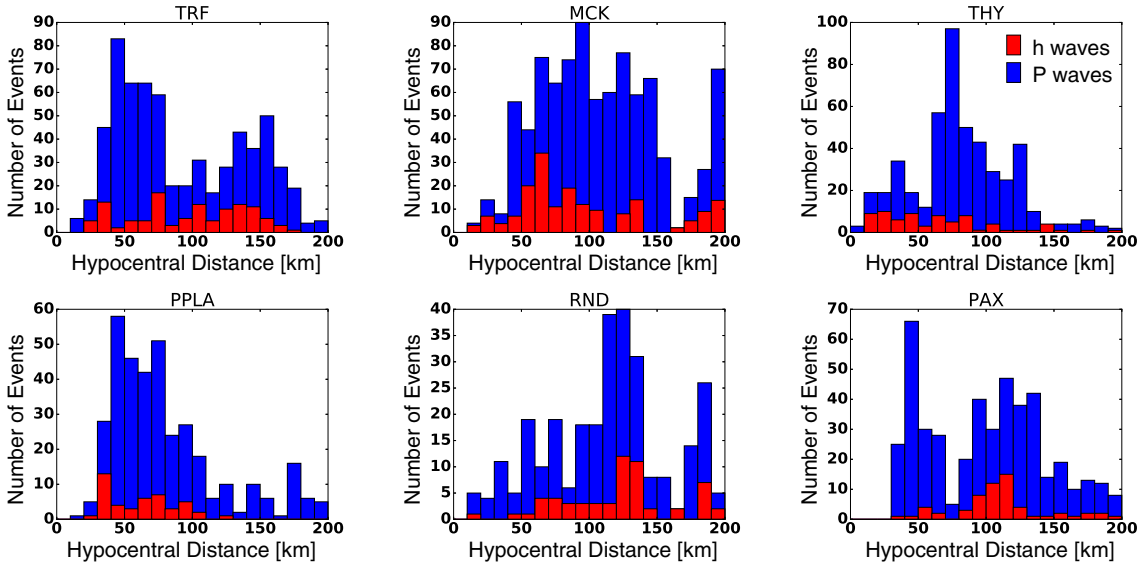

Fig. 11. Head wave detection distributions (red) for events in hypocentral distance bins; P wave detections are shown for reference in blue. Refer to Fig. 4b for station locations. Stations PPLS, MCK, and THY are north of the fault and show head waves mostly from nearer events. Stations RND and PAX south of the fault observe head waves mostly from distant events. (For interpretation of the references to color in this figure legend, the reader is referred to the web version of this article.)

results are consistent with the control group, though there are more detections at stations further west due to the increased event coverage spatially.

As further validation of the automated head wave picks, we examine the horizontal particle motions of several event-station pairs (Supp. Fig. S1). This analysis takes advantage of the fact that direct P waves are polarized along the station-event backazimuth, while the head wave will be obliquely polarized to the backazimuth (Allam et al., 2014b). We find that the picks on both sides of the fault produce particle motion consistent with fault zone head waves. At station MCK on the northern side of the fault, a distant event (Fig. S1 left) produces a first-arriving direct P wave polarized along the backazimuth, while a nearby event produces a first-arriving head wave (Fig. S1 right). Station TRF, also north of the fault, records head waves for events both east and west of the station (Fig. S2). In contrast, station PAX south of the fault records a very distinct P wave for a nearby event (Fig. S3 left), but a clear head wave for a more distant event. Station DHY, also south of the fault, shows only a P wave for a distant off-fault event (Fig. S4 left), while a near-fault event at a similar distance produces clear head waves (Fig. S4 right).

To explore the relationship between propagation distance and head wave occurrence, we consider the distribution of head wave detections (Fig. 11). For context, we also examine the distribution of event distances for which no head waves were detected. For stations north of the fault (PPLA, MCK, THY), the majority of head wave detections are from events < 100 km away. In contrast, the majority of head wave detections at stations south of the fault (RND, PAX) are for events at distances > 100 km. In both cases, these patterns are in spite of the fact that ample seismicity exists at all distance ranges. The lone station which doesn't follow this pattern, TRF, is likely biased by the fact that most of the nearby events are off-fault to the northwest of the station (Fig. 4b), a geometry which is unlikely to produce head waves.

4. Discussion

4.1. Deep and shallow velocity contrasts

Based on the tomography (Figs. 5 and 6) and the receiver function (Figs. 2, 3, and 10) results, the Denali fault system (including the Hines Creek and Totschunda faults) appears to have a consistent 10–15 km offset of the Moho along the entire length imaged in the present work, from longitude −153.0 to longitude −140.0. This Moho offset suggests localization of the Denali fault below the nominal seismogenic zone along the pre-existing weakness of the suture zone. To the east, the Totschunda (rather than the eastern Denali) fault displays the vertical offset and is even more sharply localized. When considered in conjunction with the seismicity patterns and measured plate motions, this suggests that the Totschunda is the more tectonically active fault and has been for some time. Both the mainshock rupture area and aftershock sequence of the 2002 Denali earthquake (e.g., Eberhart-Phillips et al., 2003) occurred along the Totschunda segment, bypassing the eastern continuation of the Denali Fault. Plate motions measured by repeated GPS surveys (Freymueller et al., 2008) show changes across the fault at every observed location; however, the Totschunda segment has not been studied using GPS stations. Our interpretation is that the Totschunda is exploiting the old and relatively weak suture zone and is the more tectonically important segment in the eastern part of the imaged region.

This Moho offset has previously been observed locally along the central Denali fault using geophysical methods including receiver functions (e.g., Ferris et al., 2003) and active-source seismic (e.g., Fuis et al., 2008), but only with localized linear arrays crossing essentially a single point of the Denali fault trace. At a broader regional scale, previous seismological works often show a contrast in velocity across the Denali fault (e.g., Eberhart-Phillips and Christensen, 2006; Ward, 2015), but lack the vertical resolution to discern it as a Moho offset rather than a crustal or mantle rheological change. Indeed, the compositional differences observed at the surface between the YCT and WCT would lead to the expectation of a shallow velocity contrast; the accreted and deformed island arc assemblage of the WCT (Nokleberg et al., 1994) is generally of higher seismic velocity in the upper crust compared to the largely metamorphic YCT (Mortensen, 1992; Plafker and Berg, 1994).

To quantify the velocity contrast across the Denali fault, we compute the average velocity at each depth from the tomographic model using all grid points within 30 km north and south of the central portion of the Denali fault. The grid points used are shown in Fig. S5a; thousands of points constrain the velocity at each depth. The result is two separate 1D seismic velocity models as a function of depth: one north of the fault and one south. We then take the ratio of the two 1D models to determine the average velocity contrast as a function of depth (Fig. 12a). In the upper 10 km, the northern side of the fault has a lower

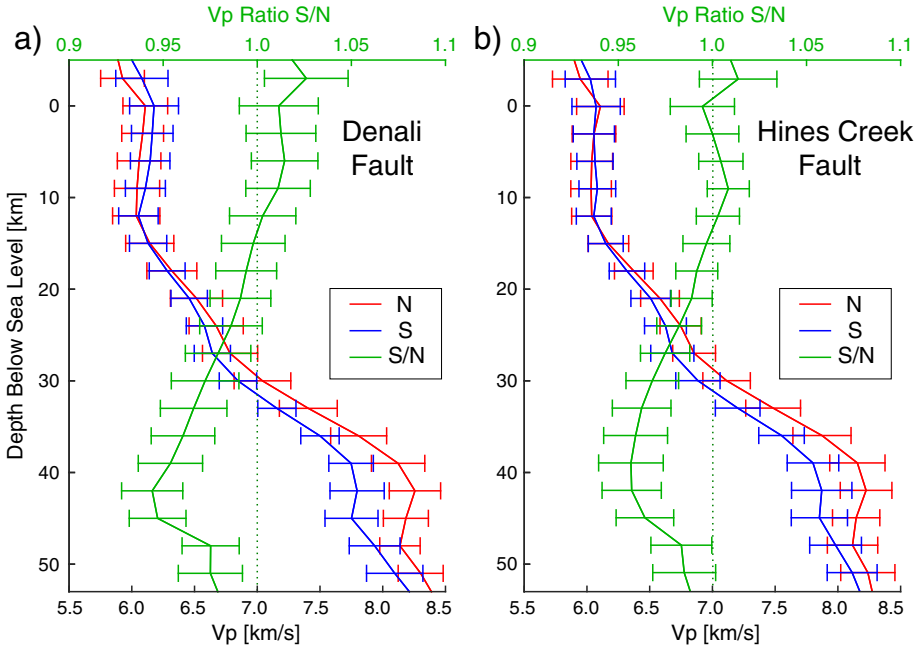

Fig. 12. The average velocity as a function of depth north (red) and south (blue) of the (a) Denali fault and (b) Hines Creek fault, with the ratio of south/north shown in green on separate x axes. The bars indicate the standard deviation of the tomographic velocities at each depth. Note that these are not error bars; the means are well-constrained by thousands of points at each depth, so the standard error (standard deviation divided by the square root of the number of points) is extremely low. The geographic locations of the tomographic grid points used to calculate the 1D models are shown in Fig. S5. For the Denali fault, the contrast in the upper 10 km is north-slow by 1–3%, while below 20 km it becomes north-fast due to the Moho offset. The Hines Creek fault has a similar Moho offset, but displays no shallow contrast. (For interpretation of the references to color in this figure legend, the reader is referred to the web version of this article.)

average velocity, creating a velocity contrast of 1–3%. Below 20 km depth, the contrast reverses, with the northern side having a 4–8% lower velocity.

Previous studies estimating Moho depth (Ferris et al., 2003; Brennan et al., 2011; Wang and Tape, 2014) suggest that the offset of the Moho is located 30 km north of the main trace of the Denali fault, perhaps along the Hines Creek fault which has been interpreted as the northernmost boundary of the WCT-YCT suture zone (Wahrhaftig et al., 1975). To test the relative importance of the Hines Creek fault in terms of velocity contrast, we repeat the 1D model analysis (grid points shown in Fig. S5b). The ratio of the average 1D velocity models north and south of the Hines Creek fault (Fig. 12b) show that this strand is accommodating a significant portion of the Moho offset, with a similar amplitude contrast to the Denali fault. This result is corroborated by the Moho depths derived from the receiver functions (Fig. 10), which also show changes in depth across both fault strands. Our interpretation is that the WCT-YCT suture zone is relatively broad at this location, and is expressed at depth as a gradual Moho offset across the entire zone. This result is in agreement with previous more localized linear geophysical surveys which found a gradual transition in Moho depth from the deeper WCT to the shallower YCT.

However, the shallower structural contrast is expressed entirely across the Denali fault; no shallow velocity contrast exists on the Hines Creek fault. Above 10 km depth, the southern side of the Denali fault (WCT) has the higher velocity. Though both the YCT and WCT are largely composed of metamorphic and igneous rocks with similar seismic velocities (Plafker and Berg, 1994), the lower northern velocity could possibly be due to differences in the relatively shallow Mesozoic-aged sedimentary and Tertiary igneous rocks in the central YCT. In the vicinity of the Denali fault, the YCT is composed of highly-altered Jurassic and Lower Cretaceous metasedimentary rocks (Jones et al., 1983). South of the fault, the WCT comprises several highly-altered Cretaceous units of oceanic plateau provenance (Nokleberg et al., 1994) and complicated intrusive and extrusive igneous rocks of the Cantwell Formation (Nokleberg et al., 1992) which likely have higher seismic velocities than the Mesozoic sedimentary rocks.

4.2. Fault zone head waves

The depth profile of the velocity contrast (Fig.12), due to the shallow geology and deeper Moho offset, explains the distribution of fault zone head waves on both sides of the fault (Fig. 11). For stations on the south side of the fault (RND, PAX), most of the FZHW are from more distant events; stations on the north side of the fault (MCK, THY, PPLA) record head waves from nearby events. Our interpretation is that the P waves from distant events have deeper ray paths which are sensitive to the deeper velocity contrast, while shallower events are sensitive to the shallow contrast. This pattern may be complicated by the fact that both the Hines Creek and Denali faults express deep velocity contrasts, while only the Denali fault accommodates a shallow contrast.

To check that the head wave distribution is consistent with the tomography models, we examine the head wave moveout as a function of distance. Following previous work (Lewis et al., 2007; Allam et al., 2014b), we compute the average contrast in across-fault velocity at each station. For a simple bimaterial interface between two quarter spaces, the differential arrival time (head wave – P) grows with distance. For each station, we fit a line to the differential arrival time as a function of distance, from which we compute the velocity contrast assuming an average velocity of 5 km/s (Fig. 13). Though there is wide scatter, the measured contrasts are nearly all positive and within the 1–8% ranges computed from the average tomographic velocities (Fig. 12). Stations MCK and THY on the north side of the fault both have a ~ 2% contrast computed from events mostly < 100 km distant. Station PPLA has the highest observed contrast at 6%, in agreement with the tomography (Fig. 5; 18 km depth), implying that PPLA is located along a fault segment with a high, sharp contrast. Stations PAX and RND on the south side of the fault have ~2% contrasts, which is lower than the average contrasts at depth. The method fails for station TRF, which has a negative moveout. As discussed above, most of the events near TRF occur far away from the surface trace of the Denali fault. This suggests that the head waves observed at TRF are due to a different interface than the main Denali fault.

4.3. Comparison with other faults

The structure of the Denali fault has significant differences compared to other major crustal strike-slip faults that have been imaged tomographically at high resolution. The San Andreas fault appears to be generally underlain by a flat Moho (e.g., Tape et al., 2015; Lee et al., 2014), with larger-scale changes not coincident with either the fault

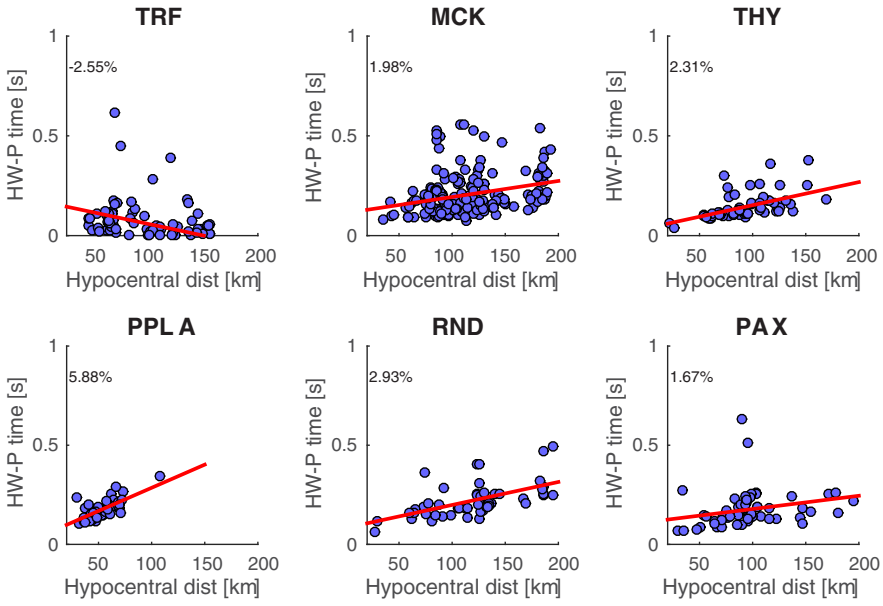

Fig. 13. Differential arrival time (head wave minus P wave) as a function of along-fault propagation distances for six stations. Stations MCK and THY are north of the fault and show similar moveout patterns. Station PPLA north of the fault is situated along a sharp, strong contrast as indicated by the moveout pattern with low scatter and few outliers, in agreement with the tomography models (Fig. 5). Stations RND and PAX south of the fault record head waves from distant events with modest velocity contrasts. This analysis fails at station TRF for reasons discussed in Section 3.4.

trace or the projected fault surfaces at depth (Plesch et al., 2007). The San Jacinto fault zone (Allam and Ben-Zion, 2012; Allam et al., 2014a; Zigone et al., 2015) has shallow low velocity zones that are prominent in the top 5 km and narrow with depth, but has no change in Moho depth across the fault. Similar low velocity zones have been observed along the Denali fault by previous local-scale seismic imaging (e.g., Brocher et al., 2004), but cannot be resolved by the tomography in the present work. The North Anatolian fault appears to be associated with a 50–100 km-wide low velocity zone which penetrates into the mantle (Fichtner et al., 2013), which the authors interpret as an ancient suture zone. No such structure exists beneath the Denali fault, despite its location along the suture between the YCT and Wrangellia. Previous inferences based on receiver functions Moho offsets along some of these other faults (e.g., Zhu, 2000; Miller et al., 2014) can be explained by accounting for the correct crustal velocity structure; i.e., an apparent Moho offset will be created by a strong shallow across-fault velocity contrast (Schulte-Pelkum and Ben-Zion, 2012; Ozakin and Ben-Zion, 2015). In the present work, however, the Moho offset is slightly accentuated when we account for the 3D structure (Fig. 3a).

Though these other faults are, like the Denali, major crustal strike-slip faults with tens to hundreds of kilometers of total offset, there are some salient differences which could explain the distinct velocity structure presently observed. The Denali fault is by far the oldest, having been active since the late Cretaceous (Ridgway et al., 2002). In addition, there is currently a fairly large relative vertical uplift (~6 mm/yr) observed in the WCT to the south of the fault (Freymueller et al., 2008). This uplift cannot simply be accounted for as being due to motion along the restraining McKinley strand (Burkett et al., 2016) because it persists > 200 km east of the McKinley strand (Freymueller et al., 2008). At the present rate, the current mantle offset could have been produced in ~15 Myr. The deep Moho offset combined with the shallow velocity contrast gives rise to a unique pattern of fault zone head wave propagation. For event-receiver distances larger than ~100 km, the waves are sensitive to the deeper velocity contrast and produce first-arriving head waves at stations on the south side of the fault. For event-receiver distances < 100 km, this pattern is reversed, with first-arriving head waves observed on the North side of the fault. Previous studies documented complicated head wave distributions owing to along-fault changes in velocity contrast (e.g., Zhao et al., 2010; Share and Ben-Zion, 2016), but this is the first observation of head wave patterns having reversal polarity contrast with depth. The depth-dependent results based on the analysis of FZHW corroborate the shallow seismic velocity contrast in the tomographic results (Fig. 12) and the receiver function Moho depth results. The derived velocity model can be used to improve the resolution and interpretation of future geophysical and geological studies in the area.

5. Conclusions

The Denali fault zone is a major crustal boundary formed along a Cretaceous-aged suture zone separating two independent crustal segments, the Wrangellia and the Yukon-Tanana Composite Terranes. Our high-resolution double-difference tomographic images show that these terranes are compositionally distinct both along-fault and with depth. To the east, the southerly Totschunda fault—not the Denali fault—exhibits the deep Moho contrast, whereas to the west both the Denali fault and the northerly Hines Creek fault exhibit the contrast. In contrast to previous receiver function studies where apparent Moho offsets are removed by including an accurate 3D crustal velocity model (e.g., Ozakin and Ben-Zion, 2015), the migration using our current model strengthens the Moho offset. The spatial distribution of fault zone head wave observations is the final piece of corroborating evidence to the pattern of seismic velocities characterizing the Denali fault system. The derived seismic velocity models resolve many additional geological features than are discussed explicitly in the text. In principle, the models can be interpreted to delineate the subsurface extent of the many plutonic bodies, subsidiary faults, and smaller-scale terrane boundaries. We reserve such more detailed interpretive analyses for future work.

Acknowledgements

The study was supported by the National Science Foundation (grants EAR-1315340, EAR-1314875, and EAR-1550328). We thank Cliff Thurber, Roland Bürgmann, Fan-Chi Lin, and Keith Koper for feedback on various aspects of the work, and Pieter-Ewald Share for useful suggestions for particle motion visualization. The arrival time and waveform data were acquired from the Alaska Earthquake Center. Figures were made using GMT (Wessel and Smith, 1998), Matlab, and Python, including ObsPy (Beyreuther et al., 2010). We thank and support the Open Access and Open Source initiatives. The facilities of IRIS Data Services, and specifically the IRIS Data Management Center, were used for access to waveforms, related metadata, and/or derived products used in this study. IRIS Data Services are funded through the

Seismological Facilities for the Advancement of Geoscience and EarthScope (SAGE) Proposal of the National Science Foundation under Cooperative Agreement EAR-1261681. Data from the TA network were made freely available as part of the EarthScope USArray facility, operated by Incorporated Research Institutions for Seismology (IRIS) and supported by the National Science Foundation, under Cooperative Agreements EAR-1261681 and EAR-1251193. We thank reviewers Patrick Brennan and Ken Ridgway for thorough constructive reviews, and editor Kelin Wang for efficient handling of the manuscript.

Appendix A. Supplementary data

Supplementary data to this article can be found online at http://dx.doi.org/10.1016/j.tecto.2017.09.003.

References

Aberhan, M., 1999. Terrane history of the Canadian Cordillera: estimating amounts of latitudinal displacement and rotation of Wrangellia and Stikinia. Geol. Mag. 136 (5), 481–492. http://dx.doi.org/10.1017/s001675689900299x.

Aleinikoff, J.N., Dusel-Bacon, C., Foster, H.L., 1986. Geochronology of augen gneiss and related rocks, Yukon-Tanana terrane, east-central Alaska. Geol. Soc. Am. Bull. 97 (5), 626–637.

Allam, A.A., Ben-Zion, Y., 2012. Seismic velocity structures in the southern California plate-boundary environment from double-difference tomography. Geophys. J. Int. 190 (2), 1181. http://dx.doi.org/10.1111/j.1365-246X.2012.05544.x.

Allam, A.A., Ben-Zion, Y., Peng, Z., 2014a. Seismic imaging of a bimaterial interface along the Hayward Fault, CA, with fault zone head waves and direct P arrivals. Pure Appl. Geophys. 171 (11), 2993. http://dx.doi.org/10.1007/s00024-014-0784-0.

Allam, A.A., Ben-Zion, Y., Vernon, F., Kurzon, I., 2014b. Seismic velocity structure in the hot springs and trifurcation areas of the San Jacinto Fault Zone, California, from double-difference tomography. Geophys. J. Int. 198, 978–999.

Amand, P.S., 1957. Geological and geophysical synthesis of the tectonics of portions of British Columbia, the Yukon Territory, and Alaska. Geol. Soc. Am. Bull. 68 (10), 1343–1370.

Argus, D.F., Gordon, R.G., Heflin, M.B., Ma, C., Eanes, R.J., Willis, P., Peltier, W.R., Owen, S.E., 2010. The angular velocities of the plates and the velocity of Earth's centre from space geodesy. Geophys. J. Int. 180 (3), 913–960.

Bemis, S.P., Carver, G.A., Koehler, R.D., 2012. The Quaternary thrust system of the northern Alaska Range. Geosphere 8 (1), 196–205. http://dx.doi.org/10.1130/ges00695.1.

Bennington, N.L., Thurber, C., Peng, Z., 2013. Incorporating fault zone head wave and direct wave secondary arrival times into seismic tomography: application at Parkfield, California. J. Geophys. Res. Solid Earth 118 (3), 1008. http://dx.doi.org/10.1002/jgrb.50072.

Ben-Zion, Y., 1989. The response of two joined quarter spaces to SH line sources located at the material discontinuity interface. Geophys. J. Int. 98 (2), 213. http://dx.doi.org/10.1111/j.1365-246x.1989.tb03346.x.

Ben-Zion, Y., 1990. The response of two half spaces to point dislocations at the material interface. Geophys. J. Int. 101, 507–528.

Ben-Zion, Y., Katz, S., Leary, P., 1992. Joint inversion of fault zone head waves and direct P arrivals for crustal structure near major faults. J. Geophys. Res. Solid Earth 97 (B2), 1943–1951. http://dx.doi.org/10.1029/91jb02748.

Bemis, S.P., Weldon, R.J., Carver, G.A., 2015. Slip partitioning along a continuously curved fault: quaternary geologic controls on Denali fault system slip partitioning, growth of the Alaska Range, and the tectonics of south-central Alaska. Lithosphere 7 (3), 235–246.

Beyreuther, M., Barsch, R., Krischer, L., 2010. ObsPy: a python toolbox for seismology. Seismol. Res. Lett. 81 (3), 530–533. http://dx.doi.org/10.1785/gssrl.81.3.530.

Bhat, H.S., Dmowska, R., Rice, J.R., Kame, N., 2004. Dynamic slip transfer from the Denali to Totschunda faults, Alaska: testing theory for fault branching. Bull. Seismol. Soc. Am. 94 (6B), S202–S213.

Biggs, J., Wright, T., Lu, Z., 2007. Multi-interferogram method for measuring interseismic deformation: Denali Fault, Alaska. Geophys. J. Int. 170 (3), 1165–1179. http://dx.doi.org/10.1111/j.1365-246x.2007.03415.x.

Brennan, P., Gilbert, H., Ridgway, K., 2011. Crustal structure across the central Alaska Range: anatomy of a Mesozoic collisional zone. Geochem. Geophys. Geosyst. 12 (4). http://dx.doi.org/10.1029/2011gc003519.

Brocher, T.M., Fuis, G.S., Lutter, W.J., 2004. Seismic velocity models for the Denali fault zone along the Richardson Highway, Alaska. Bull. Seismol. Soc. Am. 94 (6B), S85–S106. http://dx.doi.org/10.1785/0120040615.

Brogan, G.E., Cluff, L.S., Korringa, M.K., Slemmons, D.B., 1975. Active faults of Alaska. Tectonophysics 29 (4), 73–85.

Bulut, F., Ben-Zion, Y., Bohnhoff, M., 2012. Evidence for a bimaterial interface along the Mudurnu segment of the North Anatolian Fault Zone from polarization analysis of P waves. Earth Planet. Sci. Lett. 327, 17–22.

Burkett, C.A., Bemis, S.P., Benowitz, J.A., 2016. Along-fault migration of the Mount McKinley restraining bend of the Denali fault defined by late Quaternary fault patterns and seismicity, Denali National Park & Preserve, Alaska. Tectonophysics 693, 489–506.

Christensen, D., Abers, G., Hansen, R., 1999. Broadband Experiment Across the Alaska Range. International Federation of Digital Seismograph Networkshttp://dx.doi.org/10.7914/SN/XE_1999.

Doser, D.I., 2004. Seismicity of the Denali-Totschunda fault zone in Central Alaska (1912–1988) and its relation to the 2002 Denali fault earthquake sequence. Bull. Seismol. Soc. Am. 94 (6B), S132–S144.

Dusel-Bacon, C., Lanphere, M.A., Sharp, W.D., Layer, P.W., Hansen, V.L., 2002. Mesozoic thermal history and timing of structural events for the Yukon-Tanana Upland, east-central Alaska: $^{40}Ar/^{39}$ data from metamorphic and plutonic rocks. Can. J. Earth Sci. 39 (6), 1013–1051.

Eberhart-Phillips, D., Haeussler, P.J., Freymueller, J.T., Frankel, A.D., Rubin, C.M., Craw, P., Ratchkovski, N.A., et al., 2003. The 2002 Denali fault earthquake, Alaska: a large magnitude, slip-partitioned event. Science 300 (5622), 1113–1118.

Eberhart-Phillips, D., Christensen, D.H., Brocher, T.M., Hansen, R., Ruppert, N.A., Haeussler, P.J., Abers, G.A., 2006. Imaging the transition from Aleutian subduction to Yakutat collision in central Alaska, with local earthquakes and active source data. J. Geophys. Res. Solid Earth 111 (B11), 208–219. http://dx.doi.org/10.1029/2005jb004240.

Ferris, A., Abers, G.A., Christensen, D.H., 2003. High resolution image of the subducted Pacific (?) plate beneath central Alaska, 50–150 km depth. Earth Planet. Sci. Lett. 214 (3), 575–588.

Fichtner, A., Saygin, E., Taymaz, T., Cupillard, P., 2013. The deep structure of the North Anatolian fault zone. Earth Planet. Sci. Lett. 373, 109–117.

Fitzgerald, P.G., Sorkhabi, R.B., Redfield, T.F., Stump, E., 1995. Uplift and denudation of the central Alaska Range: a case study in the use of apatite fission track thermochronology to determine absolute uplift parameters. J. Geophys. Res. Solid Earth 100 (B10), 20175–20191.

Fitzgerald, P.G., Roeske, S.M., Benowitz, J.A., Riccio, S.J., 2014. Alternating asymmetric topography of the Alaska range along the strike-slip Denali fault: strain partitioning and lithospheric control across a terrane suture zone. Tectonics 33 (8), 1519–1533. http://dx.doi.org/10.1002/2013tc003432.

Freymueller, J.T., Woodard, H., Cohen, S.C., 2008. Active deformation processes in Alaska, based on 15 years of GPS measurements. In: Active Tectonics and Seismic Potential of Alaska. 1. pp. 1–42. http://dx.doi.org/10.1029/179gm02.

Fuis, G.S., Moore, T.E., Plafker, G., Brocher, T.M., 2008. Trans-Alaska Crustal Transect and continental evolution involving subduction underplating and synchronous foreland thrusting. Geology 36 (3), 267–270. http://dx.doi.org/10.1130/g24257a.1.

Gilbert, H., 2012. Crustal structure and signatures of recent tectonism as influenced by ancient terranes in the western United States. Geosphere 8 (1), 141–157.

Hansen, V.L., 1990. Yukon-Tanana terrane: a partial acquittal. Geology 18 (4), 365–369.

Hansen, S.M., Dueker, K.G., Stachnik, J.C., 2013. A rootless Rockies—support and lithospheric structure of the Colorado Rocky Mountains inferred from CREST and TA seismic data. Geochem. Geophys. Geosyst. 14 (8), 2670–2695. http://dx.doi.org/10.1002/ggge.20143.

Hayes, G.P., Wald, D.J., Johnson, R.L., 2012. Slab1.0: a three-dimensional model of global subduction zone geometries. J. Geophys. Res. Solid Earth 117 (B1), B01207–B01221. http://dx.doi.org/10.1029/2011jb008524.

Jones, D.L., Silberling, N.J., Hillhouse, J., 1977. Wrangellia—A displaced terrane in northwestern North America. Can. J. Earth Sci. 14 (11), 2565–2577.

Jones, D.L., Silberling, N.J., Gilbert, W.J., Coney, P.J., 1983. Tectono-stratigraphic Map and Interpretive Bedrock Geologic Map of the Mount McKinley Region, Alaska. http://dx.doi.org/10.14509/2342. (83-11).

Kissling, E., Lahr, J.C., 1991. Tomographic image of the Pacific slab under southern Alaska. 84 (2), 297–315.

Koehler, R.D., Burns, R.E., Combellick, R.P., 2012. Quaternary Faults and Folds in Alaska: A Digital Database. http://dx.doi.org/10.14509/23944.

Lee, E.-J., Chen, P., Jordan, T.H., Maechling, P.B., Denolle, M.A.M., Beroza, G.C., 2014. Full-3-D tomography for crustal structure in Southern California based on the scattering-integral and the adjoint-wavefield methods. J. Geophys. Res. Solid Earth 119 (8), 6421–6451. http://dx.doi.org/10.1002/2014JB011346.

Lévêque, J.-J., Rivera, L., Wittlinger, G., 1993. On the use of the checker-board test to assess the resolution of tomographic inversions. Geophys. J. Int. 115 (1), 313–318.

Lewis, M.A., Ben-Zion, Y., McGuire, J., 2007. Imaging the deep structure of the San Andreas Fault south of Hollister with joint analysis of fault zone head and direct P arrivals. Geophys. J. Int. 169 (3), 1028–1042. http://dx.doi.org/10.1111/j.1365-246x.2006.03319.x.

Ligorría, J.P., Ammon, C.J., 1999. Iterative deconvolution and receiver-function estimation. Bull. Seismol. Soc. Am. 89 (5), 1395–1400.

Martin-Short, R., Allen, R.M., Bastow, I.D., 2016. Subduction geometry beneath south central Alaska and its relationship to volcanism. Geophys. Res. Lett. 43 (18), 9509–9517.

Matmon, A., Schwartz, D.P., Haeussler, P.J., Finkel, R., 2006. Denali fault slip rates and Holocene–late Pleistocene kinematics of central Alaska. Geology 34 (8), 645–648. http://dx.doi.org/10.1130/g22361.1.

McGuire, J., Ben-Zion, Y., 2005. High-resolution imaging of the Bear Valley section of the San Andreas Fault at seismogenic depths with fault-zone head waves and relocated seismicity. Geophys. J. Int. 163 (1), 152–164. http://dx.doi.org/10.1111/j.1365-246x.2005.02703.x.

Meltzer, A., Rudnick, R., Zeitler, P., Levander, A., Humphreys, G., Kalrstrom, K., Ekstrom, E., 1999. The USArray initiative. Geol. Soc. Am. Today 9, 8–10.

Meyers, E.V., Christensen, D.H., Abers, G.A., Stachnik, J.C., 2000. Broadband (seismic) experiment across the Alaska range (BEAAR) to determine the crustal and upper mantle structure beneath central Alaska. Eos 81, F877.

Miller, M.S., Zhang, P., Dolan, J.F., 2014. Moho structure across the San Jacinto fault zone: insights into strain localization at depth. Lithosphere 6 (1), 43–47. http://dx.doi.org/10.1130/l295.1.

Mortensen, J.K., 1992. Pre-mid-Mesozoic tectonic evolution of the Yukon-Tanana terrane, Yukon and Alaska. Tectonics 11 (4), 836–853. http://dx.doi.org/10.1029/91tc01169.
Najdahmadi, B., Bohnhoff, M., Ben-Zion, Y., 2016. Bimaterial interfaces at the Karadere segment of the North Anatolian Fault, northwestern Turkey. J. Geophys. Res. Solid Earth 121 (2), 931–950.
Nokleberg, W.J., Jones, D.L., Silberling, N.J., 1985. Origin and tectonic evolution of the Maclaren and Wrangellia terranes, eastern Alaska Range, Alaska. Geol. Soc. Am. Bull. 96 (10), 1251–1270.
Nokleberg, W.J., Aleinikoff, J.N., Lange, I.M., Silva, S.R., 1992. Preliminary geologic map of the Mount Hayes quadrangle, eastern Alaska Range, Alaska. In: US Geological Survey Maps, pp. 92–594. http://dx.doi.org/10.14509/2346.
Nokleberg, W.J., MollStalcup, E.J., Miller, T.P., Brew, D.A., 1994. Tectonostratigraphic terrane and overlap assemblage map of Alaska. In: US Geological Survey Maps, pp. 94–194. http://dx.doi.org/10.1029/gd019p0323.
Ozakin, Y., Ben-Zion, Y., 2015. Systematic receiver function analysis of the Moho geometry in the Southern California Plate-Boundary region. Pure Appl. Geophys. 172 (5), 1167–1184. http://dx.doi.org/10.1007/s00024-014-0924-6.
Park, J., Levin, V., 2016. Anisotropic shear zones revealed by backazimuthal harmonics of teleseismic receiver functions. Geophysical Supplements to the Monthly Notices of the Royal Astronomical Society 207 (2), 1216–1243.
Pavlis, T.L., Sisson, V.B., Foster, H.L., Nokleberg, W.J., 1993. Mid-Cretaceous extensional tectonics of the Yukon-Tanana Terrane, Trans-Alaska Crustal Transect (TACT), east-central Alaska. Tectonics 12 (1), 103–122. http://dx.doi.org/10.1029/92tc00860.
Plafker, G., Berg, H.C., 1994. The geology of Alaska. In: The Geology of Alaska, pp. 389–449. http://dx.doi.org/10.1130/dnag-gna-g1.389.
Plafker, G., Naeser, C.W., Zimmerman, R.A., Lull, J.S., Hudson, T., 1992. Cenozoic uplift history of the Mount McKinley area in the central Alaska Range based on fission-track dating. USGS Bull. 2041, 202–212.
Plesch, A., Shaw, J.H., Benson, C., Bryant, W.A., 2007. Community fault model (CFM) for southern California. Bull. Seismol. Soc. Am. 97 (6), 1793–1802. http://dx.doi.org/10.1785/0120050211.
Qi, C., Zhao, D., Chen, Y., 2007. Search for deep slab segments under Alaska. Phys. Earth Planet. Inter. 165 (1), 68–82.
Ratchkovski, N.A., Hansen, R.A., 2002. New constraints on tectonics of interior Alaska: earthquake locations, source mechanisms and stress regime. Bull. Seismol. Soc. Am. 92, 998–1014.
Ratchkovski, N.A., Wiemer, S., Hansen, R.A., 2004. Seismotectonics of the Central Denali Fault, Alaska and the 2002 Denali fault earthquake sequence. Bull. Seismol. Soc. Am. 6B, S156–S174.
Richards, M.A., Jones, D.L., 1991. A mantle plume initiation model for the Wrangellia flood basalt and other oceanic plateaus. Science 254 (5029), 263–266. http://dx.doi.org/10.1126/science.254.5029.263.
Ridgway, K.D., Trop, J.M., Sweet, A.R., 1997. Thrust-top basin formation along a suture zone, Cantwell basin, Alaska Range: implications for development of the Denali fault system. Geol. Soc. Am. Bull. 109 (5), 505–523.
Ridgway, K.D., Trop, J.M., Nokleberg, W.J., 2002. Mesozoic and Cenozoic tectonics of the eastern and central Alaska Range: progressive basin development and deformation in a suture zone. Geol. Soc. Am. Bull. 114 (12), 1480–1504.
Rioux, M., Mattinson, J., Hacker, B., Kelemen, P., Blusztajn, J., Hanghøj, K., Gehrels, G., 2010. Intermediate to felsic middle crust in the accreted Talkeetna arc, the Alaska Peninsula and Kodiak Island, Alaska: an analogue for low-velocity middle crust in modern arcs. Tectonics 29, TC30015–TC30031. http://dx.doi.org/10.1029/2009TC002541.
Ross, Z.E., Ben-Zion, Y., 2014. Automatic picking of direct P, S seismic phases and fault zone head waves. Geophys. J. Int. 199 (1), 368–381. http://dx.doi.org/10.1093/gji/ggu267.
Ruppert, N.A., Ridgway, K.D., Freymueller, J.T., Cross, R.S., Hansen, R.A., 2008. Active tectonics of interior Alaska: seismicity, GPS geodesy, and local geomorphology. In: Freymueller, J.T. (Ed.), Active Tectonics and Seismic Potential in Alaska. Geophysical Monograph Series, vol. 179. pp. 109–133.
Schulte-Pelkum, V., Ben-Zion, Y., 2012. Apparent vertical Moho offsets under continental strike-slip faults from lithology contrasts in the seismogenic crust. Bull. Seismol. Soc. Am. 102 (6), 2757–2763. http://dx.doi.org/10.1785/0120120139.
Schulte-Pelkum, V., Mahan, K.H., 2014a. A method for mapping crustal deformation and anisotropy with receiver functions and first results from USArray. Earth Planet. Sci. Lett. 402, 221–233.
Schulte-Pelkum, V., Mahan, K.H., 2014b. Imaging faults and shear zones using receiver functions. Pure Appl. Geophys. 171 (11), 2967–2991. http://dx.doi.org/10.1007/s00024-014-0853-4.
Share, P.-E., Ben-Zion, Y., 2016. Bimaterial interfaces in the South San Andreas Fault with opposite velocity contrasts NW and SE from San Gorgonio Pass. Geophys. Res. Lett. 43, 10680–10687. http://dx.doi.org/10.1002/2016GL070774.
Stout, J.H., Chase, C.G., 1980. Plate kinematics of the Denali fault system. Can. J. Earth Sci. 17 (11), 1527–1537. http://dx.doi.org/10.1139/e80-160.
Tape, C., Silwal, V., Ji, C., Keyson, L., West, M.E., Ruppert, N., 2015. Transtensional tectonics of the Minto Flats fault zone and Nenana basin, central Alaska. Bull. Seismol. Soc. Am. 105 (4), 2081–2100.
Thurber, C., Eberhart-Phillips, D., 1999. Local earthquake tomography with flexible gridding. Comput. Geosci. 25 (7), 809–818.
Thurber, C., Zhang, H., Waldhauser, F., 2006. Three-dimensional compressional wave-speed model, earthquake relocations, and focal mechanisms for the Parkfield, California, region. Bull. Seismol. Soc. Am. 96 (4B), S38–S49. http://dx.doi.org/10.1785/0120050825.
Wahrhaftig, C., Turner, D.L., Weber, F.R., Smith, T.E., 1975. Nature and timing of movement on Hines Creek strand of Denali fault system, Alaska. Geology 3 (8), 463–466.
Wang, Y., Tape, C., 2014. Seismic velocity structure and anisotropy of the Alaska subduction zone based on surface wave tomography. J. Geophys. Res. Solid Earth 119 (12), 8845–8865. http://dx.doi.org/10.1002/2014jb011438.
Ward, K.M., 2015. Ambient noise tomography across the southern Alaskan cordillera. Geophys. Res. Lett. 42 (9), 3218–3227. http://dx.doi.org/10.1002/2015gl063613.
Wessel, P., Smith, W., 1998. New, improved version of Generic Mapping Tools released. Eos 79 (47), 579. http://dx.doi.org/10.1029/98eo00426.
Yeck, W.L., Sheehan, A.F., Schulte-Pelkum, V., 2013. Sequential H-κ stacking to obtain accurate crustal thicknesses beneath sedimentary basins. Bull. Seismol. Soc. Am. 103 (3), 2142–2150.
Zhang, H., Thurber, C.H., 2003. Double-difference tomography: the method and its application to the Hayward fault, California. Bull. Seismol. Soc. Am. 93 (5), 1875–1889.
Zhang, H., Thurber, C.H., Shelly, D., Ide, S., Beroza, G.C., 2004. High-resolution subducting-slab structure beneath northern Honshu, Japan, revealed by double-difference tomography. Geology 32 (4), 361–364. http://dx.doi.org/10.1130/g20261.2.
Zhao, P., Peng, Z., Shi, Z., Lewis, M.A., Ben-Zion, Y., 2010. Variations of the velocity contrast and rupture properties of M6 earthquakes along the Parkfield section of the San Andreas Fault. Geophys. J. Int. 180 (2), 765–780. http://dx.doi.org/10.1111/j.1365-246x.2009.04436.x.
Zhu, L., 2000. Crustal structure across the San Andreas Fault, southern California from teleseismic converted waves. Earth Planet. Sci. Lett. 179 (1), 183–190.
Zigone, D., Ben-Zion, Y., Campillo, M., Roux, P., 2015. Seismic tomography of the Southern California plate boundary region from noise-based Rayleigh and Love waves. Pure Appl. Geophys. 172 (5), 1007–1032. http://dx.doi.org/10.1007/s00024-014-0872-1.